

Creation of an isolated turbulent blob fed by vortex rings

Takumi Matsuzawa,¹ Noah P. Mitchell,¹ Stephane Perrard,¹ and William T.M. Irvine^{1,2}

¹*James Franck Institute and Department of Physics, University of Chicago, Chicago, IL 60637, USA*

²*Enrico Fermi Institute, University of Chicago, Chicago, IL 60637, USA*

(Dated: July 27, 2022)

Turbulence is hard to control. A plethora of experimental methods have been developed to generate this ephemeral state of matter, leading to fundamental insights into its statistical and structural features as well as its onset at ever higher Reynolds numbers. In all cases however, the central role played by the material boundaries of the apparatus poses a challenge on understanding what the turbulence has been fed, and how it would freely evolve. Here, we build and control a confined state of turbulence using only elemental building blocks: vortex rings. We create a stationary and isolated blob of turbulence ($Re_\lambda = 50 - 300$) in a quiescent environment, initiated and sustained solely by vortex rings. We assemble a full picture of its three-dimensional structure, onset, energy budget and tunability. Crucially, the incoming vortex rings can be endowed with conserved quantities, such as helicity, which can then be controllably transferred to the turbulent state. Our ‘one eddy at a time’ approach paves the way for sculpting turbulent flows much as a state of matter, ‘printing’ it at a targeted position, localizing it, and ultimately harnessing it. Our work paves the way to gaining a complete picture of this ephemeral state of flow.

Vorticity, which measures the local rotation rate of a fluid, is the building block of flow. In its absence, any fine structure in an incompressible flow decays rapidly with distance from material boundaries. Conversely, injection of vorticity can power complex bulk flows [1, 2], the quintessential example being the iconic multi-scale liveliness of turbulence. Canonical methods of generating turbulence rely on the spontaneous shedding of vorticity from boundaries [3–10], be it of pipes [11–14], grids [15–18], or spinning plates [19–21]. This makes it hard to control, or have detailed knowledge of, the fabric of the injected vorticity. It also often couples the turbulence to boundaries, posing a challenge to study its unconstrained evolution. Yet, our most basic models of turbulence are cast in terms of vorticity alone, with no reference to walls.

Knowing the structure of the vorticity that feeds turbulence is fundamental to a full understanding of turbulence because it determines the inviscid invariants including the amount of energy, helicity, linear impulse, and angular impulse that are injected into turbulence. The balance of the latter two invariants, for example, might lead to different types of turbulence in the large scales [22], and have been proposed to rule the decay of turbulence [23–26]. To make it possible to address these fundamental questions, we set out to build and sustain an isolated region of turbulence far away from boundaries, while controlling the injection of inviscid conserved quantities and fully observing its free evolution.

Vortex loops are a natural candidate to this end. A vortex ring is readily generated by impulsively drawing water through an orifice in a tank (Figure 1b). Seeding the water with bubbles reveals the coherent motion of the ring as it travels across the tank carrying its ‘atmosphere’ as it propagates (Figure 1c). Such a ring can, in an ideal fluid, travel infinitely far away from the boundaries. In real fluids, vortex rings eventually decay via viscous processes, or break down due to instabilities [27–29]. Nonetheless, they coherently carry their vorticity,

and associated inviscid invariants, far from the boundaries that gave rise to them.

We set out to combine vortex loops like LEGO blocks, firing them together to ‘print’ a stationary region of turbulence in the center of our tank (Figure 1a). As demonstrated in iconic vortex collision experiments [30–32], recently revisited as a minimal means to understand the inertial cascade in real space [32–35], two vortex rings fired together can multiply into a series of smaller rings, giving rise to turbulence. Figure 1e shows a version of this experiment using a pair of vortices created by drawing fluid into our tank through opposing orifices (Figure 1d). The rings, visualized using bubbles, approach each other, stretch and recombine into smaller, outwardly propagating rings. This example however, also highlights the tendency of colliding vortices to divide and redirect, escaping confinement. The situation is unchanged in the case of four vortices (Figure 1f) or eight (Figure 2a-d). This generic behavior of vortices colliding, reconnecting, and escaping challenges the idea that a blob of turbulence can be printed and confined at a target position.

In a naïve attempt to hold the escaping vorticity in place, we fired subsequent sets of eight vortex rings at repeating intervals so that the outgoing vortices would interact with the in-going vortices. To image the flow we use a combination of Particle Imaging Velocimetry (PIV), seeded bubble tracking, and 3D Particle Tracking Velocimetry (PTV). (See SI section II for a detailed description of the acquisition and visualization processes.) At a low frequency ($f = 0.2\text{Hz}$), we observe a simple repetition of the single-shot reconnection dynamics (Figure 2a-d); coherent vorticity comes in and leaves. However, when the frequency is sufficiently high to enable the outgoing vortex rings to interact with the incoming rings, a novel state with a remarkably different vorticity distribution emerges (Figure 2e-g, $f = 4\text{Hz}$).

In this new state, vorticity is confined, and is evenly distributed within an approximately spherical region.

The developed flow inside the blob is in stark contrast to its surroundings which remain relatively quiescent. The blob is sustained as long as the vortex rings are injected. Both energy and enstrophy averaged over the measured plane indicate the comparative steadiness of the state (Figure 2h) with weak dependence on the periodic forcing.

In Figure 3a we show a Reynolds decomposition of this chaotic flow into mean and fluctuating components: $U_i = \langle U_i \rangle + u_i$. The blue cloud represents the average energy associated with the fluctuations and occupies the central region alone, whereas the yellow clouds represent the mean flow energy, associated with the paths along which the vortex rings are fed. We find that the flow inside the blob is dominated by fluctuations ($\langle u^2 \rangle / \langle U \rangle^2 \approx 10^{1.5} - 10^3$) whereas the flow outside the blob is dominated by coherent flow. Furthermore, the velocity fluctuations inside the blob are only weakly dependent of the forcing phase, whereas the coherent flow outside the blob is phase-dependent, reflecting the laminar motion of the vortex rings. The temporally-and-radially averaged profiles of both fluctuating energy and enstrophy are approximately constant up to a radius R_{blob} (see SI section VI A), and decay rapidly for $r > R_{\text{blob}}$, and can be parameterized approximately as a power law with an exponent r^{-4} . The local dissipation rate $\epsilon_{s_{ij}}(r) = 2\nu \langle s_{ij} s_{ij} \rangle$ also possesses the same radial profile as energy and enstrophy (Figure 3b) where $s_{ij} = (\partial_j u_i + \partial_i u_j)/2$.

To investigate the character of the flow inside the blob, we compute the fluctuating energy spectrum and the second-order structure function. PIV measurements are inherently limited at small scales by image resolution and at large scales by the finite field of view. To span the full range of scales in our turbulent flow, we performed 2D PIV measurements at three levels of magnification (Figure 3d, spatial resolutions: $\Delta_x = 0.5, 1.3, 2.4\text{mm} = 2.4\eta, 6.2\eta, 11.4\eta$) and stitched the results together by taking into account the spectral leakage and low-pass filtering effects of PIV. With 3D PTV, we measure a one-dimensional energy spectrum on the slice that cuts the middle of the turbulent blob with a spatial resolution of $\Delta_x = 3.0\text{mm} = 14.4\eta$. In addition, the resulting 4D velocity field offers a direct computation of a three-dimensional energy spectrum without the assumption of isotropy (see SI section VII). The resulting one-dimensional energy spectrum $E_{11}(\kappa_1)$ and the second-order structure function D_{LL} of the fluctuating component of the flow are shown in Figure 3e-f. Our measurements at the three levels of magnification agree where their ranges of validity overlap. The rescaled spectrum is in excellent agreement with the universal curve obtained by grid turbulence and turbulent boundary layer experiments [9]. Similarly, the second-order longitudinal structure function when rescaled by the $2/3$ power law in the inertial sub-range is consistent with that of homogeneous isotropic turbulence.

Our spectra and structure function support the notion that the flow inside the blob is turbulent and there-

fore that its statistical properties can be captured by a dissipation rate ϵ_0 and an integral scale \mathcal{L} [36, 37], together with the fluid viscosity ν . While the value of ϵ_0 is notoriously challenging to measure [38, 39], it can be inferred from the local strain rate measurements, from fitting the measured spectrum to the universal curve, or by fitting the peak value in the scaled second order structure function [38]. As discussed in SI section VI, we find all three methods are in agreement when computed on our median-filtered, spatio-temporally resolved velocity fields. The corresponding value of the Kolmogorov length $\eta = (\nu^3/\epsilon_0)^{1/4}$ is shown in Figure 3e. A measurement of the turbulent r.m.s. velocity $u' = \sqrt{\langle u_i u_i \rangle / 3}$ in turn provides the estimate of the integral length scale $\mathcal{L} = u'^3/\epsilon_0$.

How are the properties of this turbulent blob controlled by the incoming vortex rings? As shown in Figure 3e, we find the value of the integral length-scale to be close to that of the blob diameter $2R_{\text{blob}}$, suggesting both blob radius and integral length-scales are determined by the largest scale in the incoming vortex rings. This observation is supported by repetitions of our experiment in which we varied frequency of injection of the incoming vortex rings and found no change in either \mathcal{L} or R_{blob} . A repetition of our experiment in which the incoming vortex ring radius was halved, resulted instead in a halving of both \mathcal{L} or R_{blob} (see SI section X).

The smallest (Kolmogorov) length-scale of the turbulent blob η (Figure 3e) has by contrast little relation to the vortex ring radius, and is instead strongly affected by the incoming vortex ring energy and frequency of injection. This is consistent with the notion that at the smallest length-scales turbulence ‘forgets’ about the large-scale forcing that gave rise to it and the velocity field depends only on energy flux ϵ_0 and viscosity ν . We thus turn our attention to the balance of energy in our system.

Because the flow is at dynamical equilibrium, the dissipated power must match the power injected by the vortex rings. If we neglect any residual dissipation due to the mean flow, the energy balance is

$$4\pi\rho \int \epsilon(r)r^2 dr \approx 8K_{\text{ring}}f, \quad (1)$$

where $\epsilon(r) = \epsilon_0$ if $r \leq R_{\text{blob}}$, $\epsilon_0(R_{\text{blob}}/r)^4$ otherwise. K_{ring} is the kinetic energy inside the vortex atmosphere of any one of the incoming vortices.

When integrated over all space, the L.H.S. evaluates to $16/3\pi\epsilon_0 R_{\text{blob}}^3 = 4/3\pi\epsilon_0 R_{\text{eff}}^3$, whereas if integrated up to R_{blob} we have $4/3\pi\epsilon_0 R_{\text{blob}}^3$. The R.H.S. requires knowledge of K_{ring} . When there is a vortex ring in a flow, the energy over all space K is generally the sum of the energy inside the vortex atmosphere K_{ring} and the energy of the added mass associated with the potential flow that surrounds the atmosphere K_{added} . K_{ring} can be further decomposed into the translational kinetic energy of the vortex atmosphere $K_{\text{rect}} = 4/3\pi R_{\text{atmosphere}}^3 V_{\text{ring}}^2$, and the energy associated with the rotational motion within the vortex atmosphere K_{int} . While the exact partition-

ing varies by the vortex model, the variation for K_{ring} is small (<3.3%) for realistic vortex ring models. We directly measured the energy of our vortex rings, and found $K_{\text{ring}} = (2.0 \pm 0.4)K_{\text{rect}}$ similar to $23/14K_{\text{rect}} \approx 1.6K_{\text{rect}}$ of Hill's spherical vortex (see SI section III C).

In Figure 3c we compare the measured dissipated vs injected power for a collection of blobs that are created by altering ring size, speed, and frequency of injection. The dissipated power scales linearly with the injected power, with a slope of approximately 1. A more granular accounting, e.g. including only the energy contained within the vortex ring atmosphere and computing ϵ_0 only within R_{blob} , yields a linear relationship with lower proportionality constants: 1 (total energy, total turbulent dissipation), 0.68 (energy within the incoming vortex ring atmospheres, turbulent dissipation within a sphere of radius $R_{\text{eff},i}$) and 0.33 (energy within the incoming vortex ring atmospheres, turbulent dissipation within a sphere of radius R_{blob}).

Crucially, increasing the velocity or frequency of injection increases the rate of energy dissipation while keeping the integral length-scale fixed, thereby increasing the separation of scales \mathcal{L}/η . Thus ring radius and energy injection provide independent control knobs for producing turbulence of a desired intensity localized to a given region.

The picture is in stark contrast to the single-collision experiment (Figure 2a) in which vortices come in, reconnect, and go out. At these low forcing frequencies the conversion from coherent vortex motion to turbulence is far less efficient. Even though in practice reconnections trigger energy loss within the outgoing vortices, in the limit of a single coherent collision with large separation of scales, the fraction of advected energy can be in principle 100%.

What governs the transition to a blob state? The most basic criterion is suggested by geometry: the outgoing rings will collide with the incoming rings for $f \gtrsim V_{\text{ring}}/R_{\text{ring}}$. A completely different conceptual approach is to seek to 'match' the incoming vortex 'eddies' to the turbulent state. A central idea in a turbulent cascade is that energy from each scale ℓ is transported to the next in a time $\tau_\ell \sim (\ell^2/\epsilon_0)^{1/3}$. If we demand that the time between incoming vortices $1/f$ match the timescale for the largest eddy to transfer energy down the cascade we have $1/f > \tau_\mathcal{L}$. For our fully developed turbulent blob we have $\mathcal{L} \propto R_{\text{ring}}$ (Figure 4a, $\alpha_0 = 2.17 \pm 0.13$) and $\epsilon_0 \propto V_{\text{ring}}^2 f$ (Figure 4b, $\alpha_1 = 0.35 \pm 0.02$) with proportionality constants determined in experiment. We then obtain a criterion for transition: $f_c \sim V_{\text{ring}}/R_{\text{ring}}$ with the proportionality constant determined by the independent measurements of $\mathcal{L}(R_{\text{ring}})$ and $\epsilon_0(V_{\text{ring}})$ in the fully developed turbulent state.

Figure 4e shows the time-averaged enstrophy field for experiments in which we varied both f and $V_{\text{ring}}/R_{\text{ring}}$. The transitional range predicted by matching vortex arrival intervals with the largest eddy turnover time is shown by the blue band for comparison. The relation-

ship between f_c and $V_{\text{ring}}/R_{\text{ring}}$, consistent with predictions, is qualitatively visible from the change in shape as frequency is increased. A second criterion to classify whether a given flow is in a blob state is to compute the enstrophy flux through a sphere that encloses the blob (Figure 4c). For the barotropic, incompressible fluids the integrated enstrophy flux is given by

$$\Phi_Z(t) = \int_{\partial V} \Omega^2 U_i n_i dS, \quad (2)$$

where $\Omega_i = \epsilon_{ijk} \partial_j U_k$ is vorticity. The phase-averaged (integrated) flux $\langle \Phi_Z \rangle_n$ is shown in Figure 4c for an experiment with $f < f_c$ (red) and one with $f > f_c$ (blue). The red curve shows a trough (influx > outflux), followed by a crest (influx < outflux) as the secondary rings transport enstrophy away from the considered volume. The blue curve, by contrast, shows little to no outflux. As f is increased for a given $V_{\text{ring}}/R_{\text{ring}}$, the escaping enstrophy per cycle (shaded green region in Figure 4c) smoothly decreases as the frequency is increased (Figure 4d.). This corresponds to the suppression of coherent reconnections and development of turbulence. Placing a threshold (<5% relative to the values at $f = 1\text{Hz}$) on the escaping enstrophy reveals that the transitional frequency depends on $V_{\text{ring}}/R_{\text{ring}}$ in a linear fashion (Figure 4e, orange band). The upper limit of the orange band in Figure 4e lies within 10-20% of the predicted transition frequency.

For $f > f_c$, the energy and enstrophy are completely transferred to the blob, in sharp contrast to the single shot experiment ($f \ll f_c$) in which neither are left behind nor in fact penetrate the central region. By contrast, the mass associated with the vortex atmospheres must flow in and out in equal amounts and cannot be left behind (see SI section IX). We find it interesting that the blob state can occur in the first place given this fact. Our work raises the question of whether vortex ring trains are in some sense optimally suited to confining and 'feeding' turbulence. For example, if jets were used instead of ring trains [40, 41], the input would have a higher ratio of mass to enstrophy and energy, and no blob state has been reported in this case to our knowledge [42, 43]. More generally, what types of flow 'input' lead to a maximally localized blob states vs delocalized states in which the necessary outward advection destabilizes confinement?

Finally, we explore the tunability of our turbulent blob through control of the vortex rings. The ring radius R_{ring} tunes the integral scale \mathcal{L} and the blob radius R_{blob} . Meanwhile, the energy balance sets the smallest scale of turbulence (Kolmogorov scale η) as it leads to $\epsilon_0 = \alpha_1^2 V_{\text{ring}}^2 f \sim \Gamma_{\text{ring}}^2 f / R_{\text{ring}}^2$. Hence, the separation of scales is given by $\mathcal{L}/\eta \sim (\Gamma_{\text{ring}}/\nu)^{3/4} (R_{\text{ring}} f / V_{\text{ring}})^{1/4}$, consistent with the usual relation $\mathcal{L}/\eta \sim Re_C^{3/4} \sim (u' \mathcal{L} / \nu)^{3/4}$ for general turbulence [44]. Notice that it is expressed solely by the variables of the injecting vortex rings and thus can be completely controlled by tuning their properties.

Can our approach to building a turbulent blob be harnessed to endow the turbulence with additional prop-

erties? Beyond energy, natural candidates include the inviscid invariants of impulse, angular impulse and helicity. In Figure 5 we show measurements of the total helicity in a blob created by colliding helical vortex loops in combinations that inject a total helicity of $+8\mathcal{H}_{\text{ring}}$, $-8\mathcal{H}_{\text{ring}}$ and $0\mathcal{H}_{\text{ring}}$, while injecting zero angular impulse and zero linear impulse. Although the vorticity field is not completely resolved, clearly the answer is affirmative.

We have discovered that a collection of vortex rings periodically fired together leads to a self-confining turbulent blob. This bottom-up approach to turbulence provides unique design principles to position, localize and control turbulence as a state of flow. In the canonical picture of the Richardson cascade, injection and dissipation go hand in hand at dynamical equilibrium. Nevertheless, their connection often remains elusive due to

the uncontrolled injection and evolution of vortical structures. The use of coherent, controllable vortex rings overcomes this issue, enabling us to inject fully controlled arbitrary ratios of inviscid conserved quantities. Enabled by the self-confinement effect we discovered, our experiment provides a unique control of injection and dissipation in turbulence. The turbulent blob, which can be measured in its entirety and is free to evolve in isolation, offers a playground for fundamental studies on inhomogeneous turbulence such as transfer at the turbulent/non-turbulent interface, and decay of turbulence without the boundary effects, response of turbulence to a periodic drive [45, 46], and the role of inviscid invariants such as helicity [47, 48] and angular impulse [24, 25] in turbulence. Our work views turbulence as a state of matter that can be controlled and manipulated coherently.

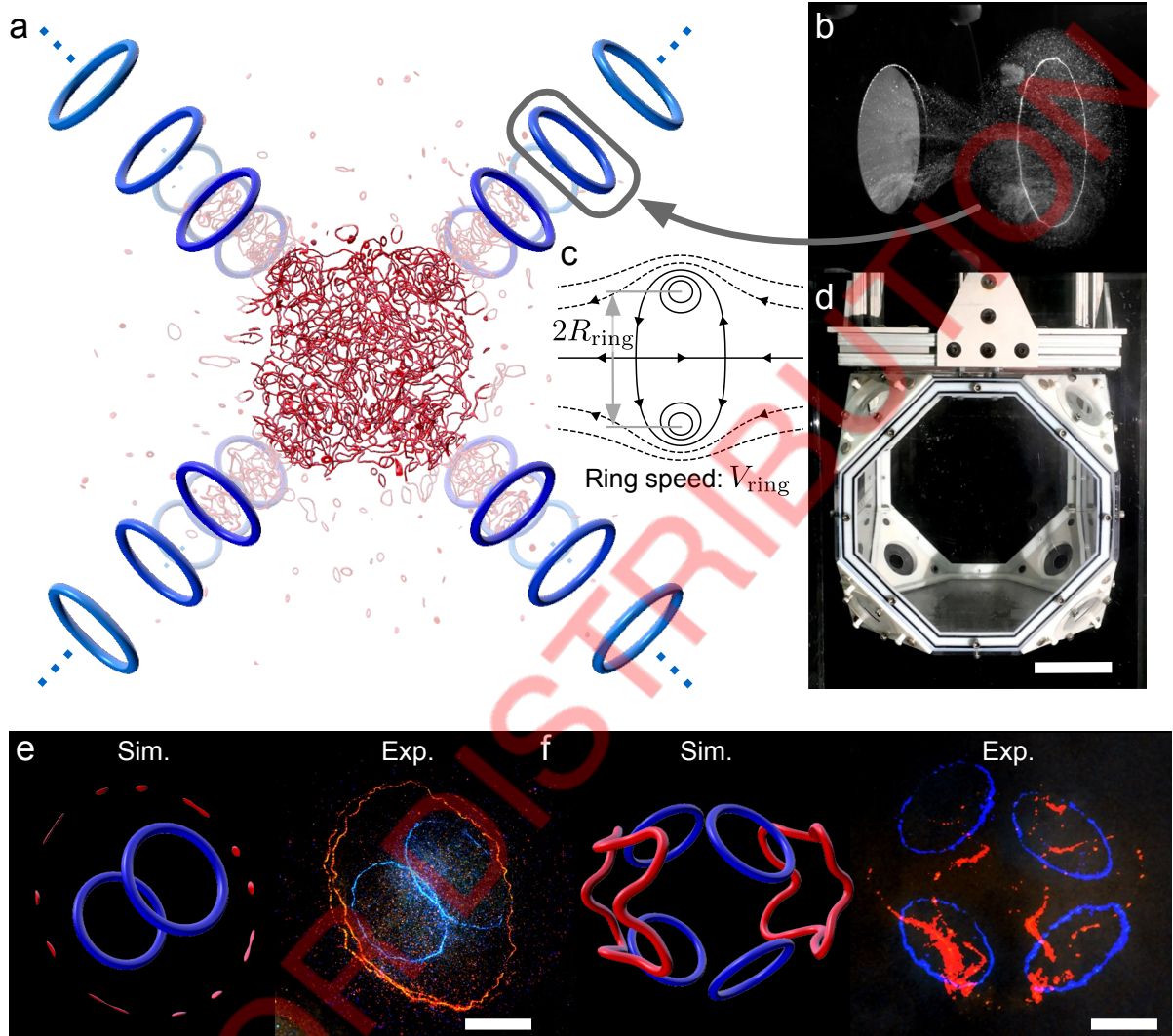


FIG. 1. Generation of turbulence using vortex rings and their resistance to confinement. (a) We envisage colliding vortex rings creates turbulence at a target location far from boundaries with a controlled injection rate of energy. (b) Extruding fluids through an orifice generates a vortex ring that is visualized by bubbles. (c) Streamline of a vortex ring in the co-moving frame. (d) A photograph of the experimental chamber where eight vortex rings are generated at its truncated faces every forcing cycle. The scale bar represents 100mm. (e-f) Vorticity resists confinement. (e) A head-on collision of two identical vortex rings (blue) generates numerous secondary rings after reconnections occur (red). The left panel shows the result of the Gross-Pitaevskii simulation, whereas the right panel shows the experiment, visualized by bubbles. The scale bar represents 30mm along the semimajor axis of the red ellipse. The red ellipse is a projection of a circle. (f) Same as (e) but the centers of the four identical rings are initially set in a square configuration (blue), ejecting two vortex loops after reconnections (red). The scale bar is the same as (e).

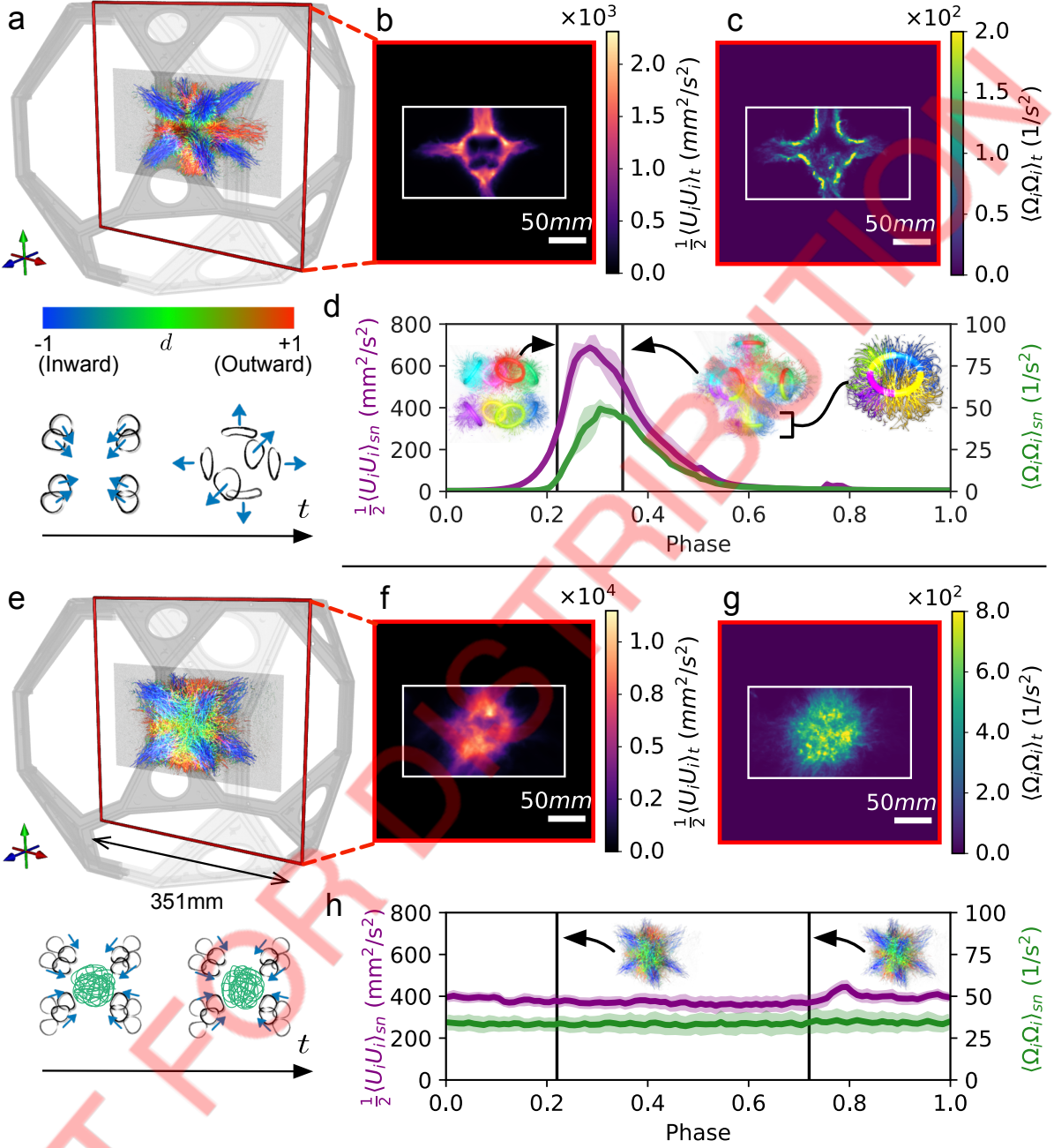


FIG. 2. Two phases emerge as eight vortex rings repeatedly collide: coherent reconnections and a confined turbulence. (a) Coherent vortex reconnections of eight vortex rings (Blue) result in six secondary rings (Red), visualized by 3D Lagrangian trajectories throughout the experiments ($t=[0, 6]$ in s). The color is the radial component of instantaneous Lagrangian speed, $d = (\vec{U}_{Lag} \cdot \hat{r}) / |\vec{U}_{Lag}|$. Opacity is weighted by speed to highlight the fast dynamics ($\alpha = \exp[-5(1 - |\vec{U}_{Lag}| / U_{Lag,0})]$ for $|\vec{U}_{Lag}| < U_{Lag,0} = 200\text{mm/s}$). ($V_{ring}/R_{ring}, f$) = (20Hz, 0.2Hz) (b-c) Time-averaged energy/ensntry on the central slice shows the trace of the secondary rings after vortex reconnections. (d) Average energy and enstrophy on the measured plane indicates the entry of the eight vortex rings, and the propagation of the secondary rings. The insets show the 3D Lagrangian trajectories before and after the reconnections. (e) Lagrangian trajectories around a turbulent blob display uniform, nearly isotropic outflow from the core. Duration: $t=[0, 6]$ in s. ($V_{ring}/R_{ring}, f$) = (20Hz, 5Hz) (f-g) Time-averaged energy/ensntry on the central slice shows an isolated region with high energy/ensntry. (h) Average energy and enstrophy on the measured plane indicates the steadiness of the state with weak dependence on the periodic forcing. The piston draws the fluids into the chamber at phase=0.77.

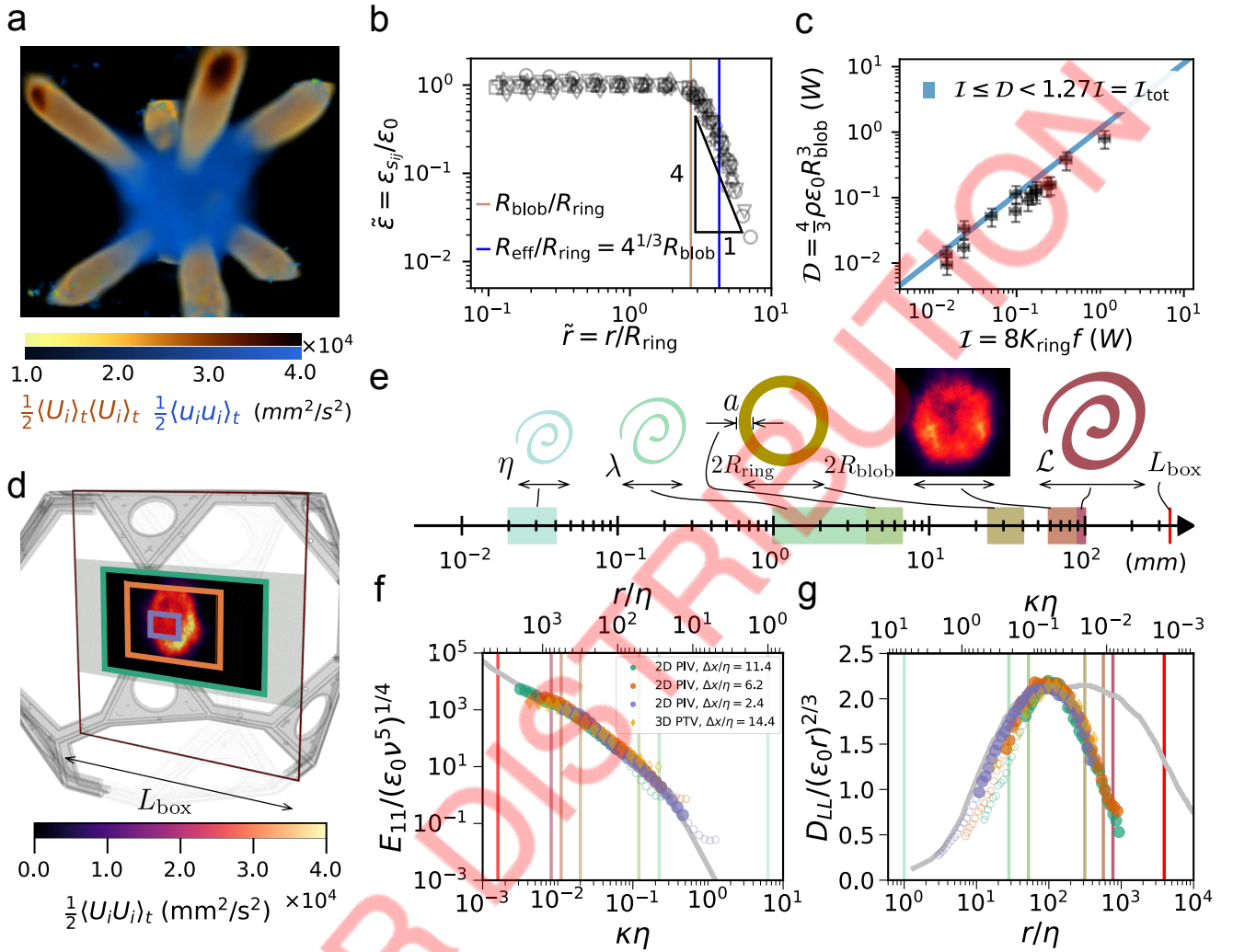


FIG. 3. Turbulent dissipation inside the blob matches the power injected by vortex rings. (a) Reynolds decomposition $U_i = \langle U_i \rangle + u_i$ reveals that the blob consists of a turbulent core with a mean flow originated from the incoming vortex rings. Yellow: the mean flow energy $\langle U_i \rangle_t \langle U_i \rangle_t / 2$. Blue: the mean turbulent energy $\langle u_i u_i \rangle_t / 2$. ($i = 1, 2, 3$) (b) Radial profile of the dissipation rate on the central plane reveals an homogeneous region up to $R = R_{blob} \approx \sqrt{6}R_{ring}$, and a tail that rapidly decays. The profile is universal over rings with different radii. (Piston stroke ratio, Piston effective stroke velocity, frequency)=($L/D, v_{eff}$ in mm/s, f in Hz)- \circ : (1.5, 196, 5), Δ : (2.0, 418, 5), ∇ : (3.0, 443, 5), \square : (3.0, 443, 7), \diamond : (3.5, 318, 5), $+$: (3.5, 594, 5), \times : (3.5, 594, 7), \star : (3.5, 594, 8) (c) Dissipated power in the sphere of radius R_{blob} linearly scales with the power injected into the blob by vortex rings. (d) Three-scale 2D PIV measurements are conducted on the plane cutting the center of the blob. ($i = 1, 2$). (e) Turbulence lengthscales with respect to the relevant geometries (blob radius R_{blob} , ring radius R_{ring} , and core diameter a). (f) Rescaled one-dimensional spectra are computed in the homogeneous region ($r \leq R_{blob}$). ($\varepsilon_0 = 6.0 \times 10^4 \text{ mm}^2/\text{s}^3$, $\nu = 1.004 \text{ mm}^2/\text{s}$, $Re_\lambda = 200$). The gray master curve is collected by multiple experiments with walls, taken from [9] ($Re_\lambda \approx 600$) as a reference. The attenuated signal due to PIV is addressed by hollow data points. (g) Rescaled second-order structure functions of the same data as (f) are shown with a reference [9] ($Re_\lambda \approx 600$).

METHODS

A. Experimental chamber and actuation

The experimental chamber is fabricated by a commercial 3D printer using ultraviolet-cured polymers (Objet VeroWhite and VeroBlack, Objet Connex 350, Stratasys), and is primarily used throughout the experiments.

A windowed chamber made of acrylic with a similar geometry is also used to measure properties of vortex rings. See Supplementary information for the design and the exact dimensions. An electric linear actuator (Copley Controls) controls the motion of the acrylic piston through signals output from a DAQ board (National Instruments.) As the piston attached to the top surface lifts up, fluid gets pulled into the chamber through the

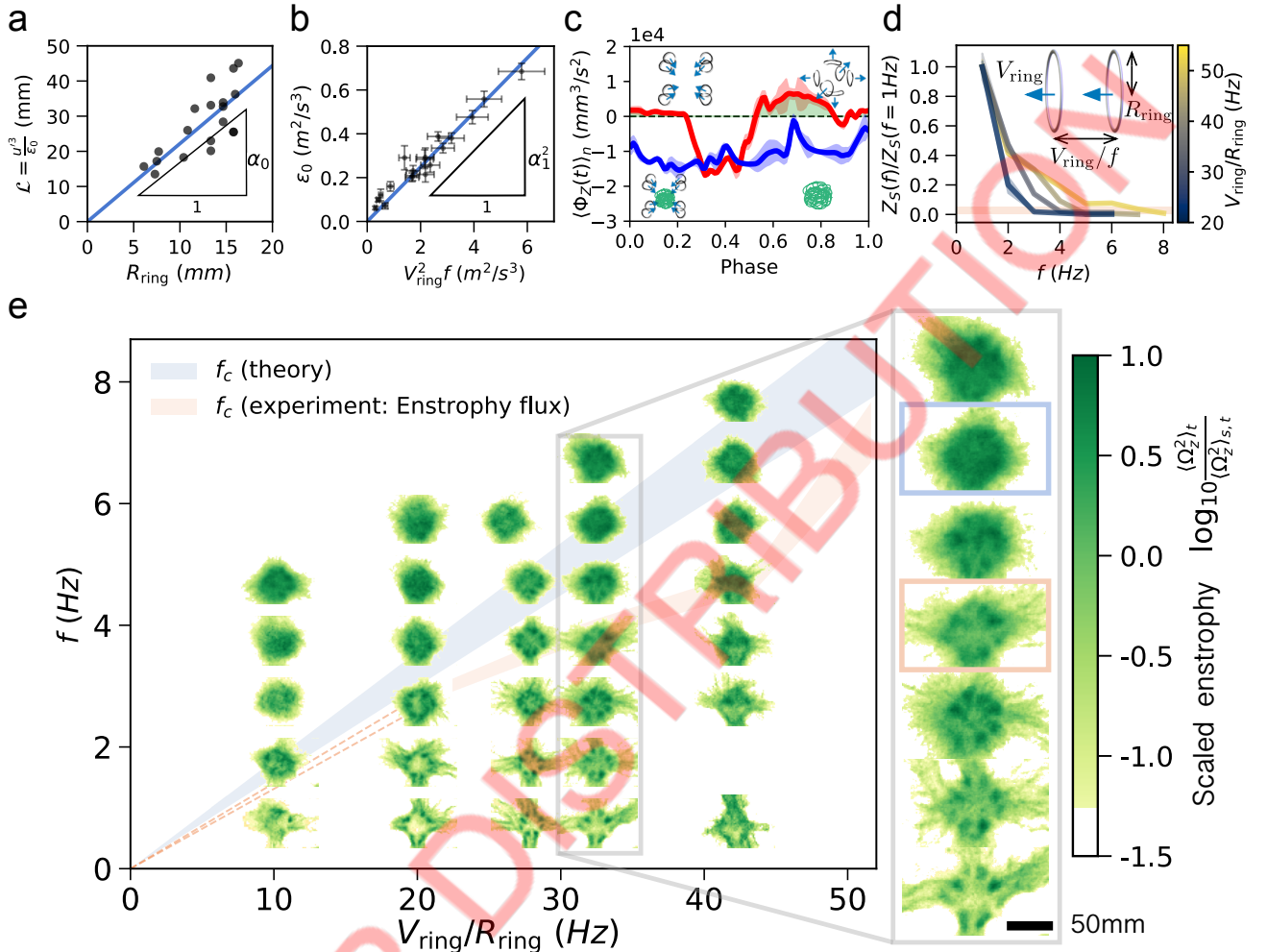


FIG. 4. $V_{\text{ring}}/(R_{\text{ring}}f)$ governs a smooth transition from coherent reconnections to turbulence. (a) Our theory predicts the transition frequency as $(\alpha_0/\alpha_1)(V_{\text{ring}}/R_{\text{ring}})$. The integral length scale \mathcal{L} is linear to the radius of the injected vortex ring R_{ring} with α_0 being a proportionality constant. (b) The second parameter α_1 is a proportionality constant between ε_0 inside the turbulent core and the power injected by vortex ring $\sim V_{\text{ring}}^2 f$. (c) Phase-averaged enstrophy flux through a sphere (radius R' enclosing a turbulent blob captures the degree of confinement ($R' = 1.25R_{\text{eff}} \approx 1.9R_{\text{blob}}$). Below the transition frequency (Red, $f = 1\text{Hz}$, $V_{\text{ring}}/R_{\text{ring}} = 20\text{Hz}$), the enstrophy flux takes positive values when the outflow is greater than inflow. Above the transition (Red, $f = 6\text{Hz}$, $V_{\text{ring}}/R_{\text{ring}} = 20\text{Hz}$), the flux is always negative throughout a cycle because the outflow is weaker than inflow (confinement). Integrating the positive regions (a green shaded region) yields escaping enstrophy per cycle $Z_S(f)$. (d) Scaled escaping enstrophy per cycle decreases as the injection frequency increases, indicating a smooth transition to a blob. The orange band corresponds to <5%. (e) Formation of a turbulent blob depends on the injection frequency and the ratio between the ring velocity and the radius. Scaled time-averaged enstrophy fields show agreements with the transition frequencies expected from our theory and measurements on the enstrophy flux. The orange band represents the frequencies that the escaping enstrophy becomes <5% of the values at $f = 1\text{Hz}$.

orifices, creating eight vortex rings travelling towards the center. A rubber flap attached to the top surface around the piston's entry point prevents unwanted flow in or out of the chamber near the piston. We use a transmissive optical encoder (EM2, US Digital) to track the motion of the piston with sub-millimeter precision. With the tracking data, we extract two important parameters regarding the properties of the vortex rings: the formation number L/D [49] (stroke ratio normalized by the orifice diameter) and the effective velocity of the piston v_{eff} . (See

Supplementary information Section II). The former governs the radius and the stability of the generated vortex ring, and is a function of the diameter of the orifices D_o and that of the piston D_p . The latter controls the speed of the vortex ring. In order to generate two sizes of the vortex rings ($R_{\text{ring}} \approx 15, 25\text{mm}$), we used two settings $(D_p, D_o) = (160.0\text{mm}, 25.6\text{mm})$, and $(56.7\text{mm}, 12.8\text{mm})$. The first setting offers a large blob of turbulence, suited for turbulent analysis through the 2D particle image velocimetry. The second setting offers a blob of turbulence

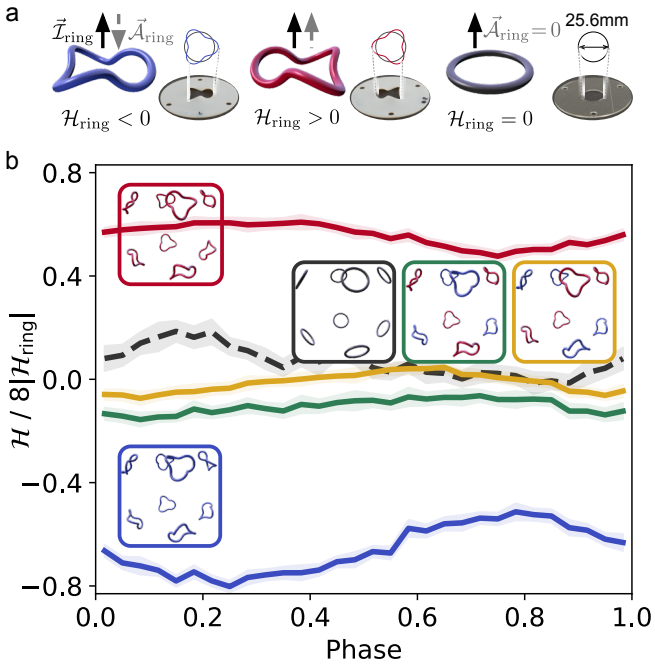


FIG. 5. Repeated collision of helical rings transfers helicity to turbulence in a controlled fashion. (a) Puffing fluids through helical and circular masks generate helical and planar rings respectively. Handedness is defined by the relative orientation of linear impulse $\vec{\mathcal{I}}_{\text{ring}}$ to angular impulse $\vec{\mathcal{A}}_{\text{ring}}$, and is tuned from antiparallel (blue) to parallel (red). (b) Helicity is transferred from helical rings to a blob of turbulence. Different configurations allow injection of helicity with different handedness. The five configurations of the measurements are illustrated in the inlet figures. (Net helicity per cycle, net angular impulse per cycle) = $(8\mathcal{H}_{\text{ring}}, 0)$ [Red: 8 Right], $(0, 0)$ [Green: 4 Right + 4 Left], $(0, 0)$ [Yellow: 4 Right + 4 Left], $(0, 0)$ [Black: 8 Planar], $(-8\mathcal{H}_{\text{ring}}, 0)$ [Blue: 8 Left]. A vortex ring of $(V_{\text{ring}}/R_{\text{ring}}, f) = (40\text{Hz}, 5\text{Hz})$ was used, and the graph shows the helicity integrated over a sphere of radius $60 \text{ mm} \approx R_{\text{blob}}$. The shade represents the standard error of the mean.

small enough with respect the illuminated volume for 3D particle tracking velocimetry to conduct the 3D flux measurements for Figure 4 without clipping the blob. We tested effects of the different thickness of the orifices on the generated rings but found that it did not qualitatively affect the dynamics.

B. Velocity field extraction

In order to characterize the flow, we illuminated fluorescent polyethylene microspheres ($d = 100\mu\text{m}$, $\rho = 1.090\text{g/cc}$, Cospheric) with a Nd:YLF single cavity diode pumped solid state laser (<40mJ/pulse, 527nm). A high-speed camera captured the beads' motion (Phantom v2515 or Phantom VEO4k, Vision Research) on a

thin laser sheet (thickness: 1mm) for 2D Particle Image Velocimetry (PIV). We varied the frame rate of the cameras, depending on the speed of the vortex ring, ranging from 250 to 3000 fps while a “quarter rule” [50] was always satisfied for the largest displacement observed. We extracted the velocity fields with a software called DaVis (LaVision, Inc.). There, we used the pyramid algorithm [51] to generate a velocity field for turbulent analysis (energy spectrum, structure function, dissipation rate, and turbulence length scales) as it was shown to extract the small-scale motion more accurately than the standard cross-correlational algorithm (WIDIM [52]).

For 4D measurements, we set up an array of three to four cameras to capture the motion of the same beads illuminated in a volume of $120\text{mm} \times 100\text{mm} \times 80\text{mm}$, created by two cylindrical lenses. The 3D particle tracking algorithm called “Shake-the-box” [53] detected $O(10^5)$ particles from the images of the different perspectives, and reconstructed their trajectories. Binning the Lagrangian velocities gave the underlying Eulerian velocity field at that frame. On average, 3-7 trajectories were present in each voxel with a width of 2.9mm. For the voxels with no trajectories, the velocity field was interpolated linearly or filled with the neighboring values.

C. 3D visualization

The Lagrangian trajectories obtained by 3D PTV were first characterized by their lifespans, traveled distances, average speeds, and positions when they were first detected. We used this information to identify the particles transported by the vortex rings. The selected particles were then visualized as pathlines using a rendering software called Houdini (SideFX). The SI movies show the pathlines combined of the four recordings for each experiment (coherent reconnections and a turbulent state.)

As for the visualization of the mean flow energy and the mean turbulent energy, we used a software called Dragonfly (Object Research Systems).

ACKNOWLEDGMENTS

The authors acknowledge Yehuda Ganen for performing the GPE simulation of a vortex ring train in Figure 1. The Chicago MRSEC is also gratefully acknowledged for access to its shared experimental facilities (US NSF grant DMR2011854). This work was supported by the Army Research Office through # W911NF-17-S-0002 and # W911NF-20-1-0117 and a Brown Fellowship. We also acknowledge LaVision Inc. for their support on the PIV and PTV processing, SideFX and Object Research Systems for granting software licenses (Houdini and Dragonfly).

- [1] M. Van Dyke, *An album of fluid motion*, Vol. 176 (Parabolic Press Stanford, 1982).
- [2] T. Von Kármán, *Aerodynamics*, Vol. 9 (McGraw-Hill New York, 1963).
- [3] A. J. Smits, B. J. McKeon, and I. Marusic, High-reynolds number wall turbulence, *Annual Review of Fluid Mechanics* **43**, 353 (2011).
- [4] R. J. Adrian, Hairpin vortex organization in wall turbulence, *Physics of Fluids* **19**, 041301 (2007).
- [5] K. T. Christensen and R. J. Adrian, Statistical evidence of hairpin vortex packets in wall turbulence, *Journal of Fluid Mechanics* **431**, 433 (2001).
- [6] J. Zhou, R. J. Adrian, S. Balachandar, and T. Kendall, Mechanisms for generating coherent packets of hairpin vortices in channel flow, *Journal of fluid mechanics* **387**, 353 (1999).
- [7] M. Acarlar and C. Smith, A study of hairpin vortices in a laminar boundary layer. part 1. hairpin vortices generated by a hemisphere protuberance, *Journal of Fluid Mechanics* **175**, 1 (1987).
- [8] M. Acarlar and C. Smith, A study of hairpin vortices in a laminar boundary layer. part 2. hairpin vortices generated by fluid injection, *Journal of Fluid Mechanics* **175**, 43 (1987).
- [9] S. G. Saddoughi and S. V. Veeravalli, Local isotropy in turbulent boundary layers at high reynolds number, *Journal of Fluid Mechanics* **268**, 333–372 (1994).
- [10] T. Theodorsen, Mechanism of turbulence, in *Proceedings of the Second Midwestern Conference on Fluid Mechanics* (1952) pp. 1–19.
- [11] O. Reynolds, Xxix. an experimental investigation of the circumstances which determine whether the motion of water shall be direct or sinuous, and of the law of resistance in parallel channels, *Philosophical Transactions of the Royal society of London* , 935 (1883).
- [12] T. Mullin, Experimental studies of transition to turbulence in a pipe, *Annual Review of Fluid Mechanics* **43**, 1 (2011).
- [13] B. Eckhardt, T. M. Schneider, B. Hof, and J. Westerweel, Turbulence transition in pipe flow, *Annu. Rev. Fluid Mech.* **39**, 447 (2007).
- [14] B. Hof, A. Juel, and T. Mullin, Scaling of the turbulence transition threshold in a pipe, *Physical review letters* **91**, 244502 (2003).
- [15] D. Hurst and J. Vassilicos, Scalings and decay of fractal-generated turbulence, *Physics of Fluids* **19**, 035103 (2007).
- [16] A. Kistler and T. Vrebalovich, Grid turbulence at large reynolds numbers, *Journal of Fluid Mechanics* **26**, 37 (1966).
- [17] G. Comte-Bellot and S. Corrsin, Simple eulerian time correlation of full-and narrow-band velocity signals in grid-generated,‘isotropic’turbulence, *Journal of Fluid Mechanics* **48**, 273 (1971).
- [18] E. Bodenschatz, G. P. Bewley, H. Nobach, M. Sinhuber, and H. Xu, Variable density turbulence tunnel facility, *Review of Scientific Instruments* **85**, 093908 (2014).
- [19] A. de la Torre and J. Burguete, Slow dynamics in a turbulent von kármán swirling flow, *Physical review letters* **99**, 054101 (2007).
- [20] R. Volk, E. Calzavarini, E. Leveque, and J.-F. Pinton, Dynamics of inertial particles in a turbulent von kármán flow, *Journal of Fluid Mechanics* **668**, 223 (2011).
- [21] R. Labb  , J.-F. Pinton, and S. Fauve, Study of the von k  rm  n flow between coaxial corotating disks, *Physics Of Fluids* **8**, 914 (1996).
- [22] P.-Å. Krogstad and P. Davidson, Is grid turbulence saffman turbulence?, *Journal of Fluid Mechanics* **642**, 373 (2010).
- [23] P. Davidson, *Turbulence: an introduction for scientists and engineers* (Oxford university press, 2015).
- [24] P. Davidson, The role of angular momentum conservation in homogeneous turbulence, *Journal of fluid mechanics* **632**, 329 (2009).
- [25] P. Saffman, Note on decay of homogeneous turbulence, *The Physics of Fluids* **10**, 1349 (1967).
- [26] L. D. Landau and E. M. Lifshitz, *Fluid Mechanics: Landau and Lifshitz: Course of Theoretical Physics, Volume 6*, Vol. 6 (Elsevier, 2013).
- [27] S. C. Crow, Stability theory for a pair of trailing vortices, *AIAA journal* **8**, 2172 (1970).
- [28] C.-Y. Tsai and S. E. Widnall, The stability of short waves on a straight vortex filament in a weak externally imposed strain field, *Journal of Fluid Mechanics* **73**, 721 (1976).
- [29] S. Le Dizes and F. Laporte, Theoretical predictions for the elliptical instability in a two-vortex flow, *Journal of Fluid Mechanics* **471**, 169 (2002).
- [30] Y. Oshima, Head-on Collision of Two Vortex Rings, *Journal of the Physical Society of Japan* **44**, 328 (1978).
- [31] T. T. Lim and T. B. Nickels, Instability and reconnection in the head-on collision of two vortex rings, *Nature* **357**, 225 (1992), number: 6375 Publisher: Nature Publishing Group.
- [32] R. McKeown, R. Ostilla-M  nico, A. Pumir, M. P. Brenner, and S. M. Rubinstein, Turbulence generation through an iterative cascade of the elliptical instability, *Science Advances* **6**, 2717 (2020), publisher: American Association for the Advancement of Science Section: Research Article.
- [33] M. P. Brenner, S. Hormoz, and A. Pumir, Potential singularity mechanism for the euler equations, *Physical Review Fluids* **1**, 084503 (2016).
- [34] R. McKeown, R. Ostilla-M  nico, A. Pumir, M. P. Brenner, and S. M. Rubinstein, Cascade leading to the emergence of small structures in vortex ring collisions, *Physical Review Fluids* **3**, 124702 (2018).
- [35] R. Ostilla-M  nico, R. McKeown, M. P. Brenner, S. M. Rubinstein, and A. Pumir, Cascades and reconnection in interacting vortex filaments, *Physical Review Fluids* **6**, 074701 (2021).
- [36] A. N. Kolmogorov, The local structure of turbulence in incompressible viscous fluid for very large Reynolds numbers, *C. R. Acad. Sci. URSS* **30**, 301 (1941).
- [37] A. N. Kolmogorov, A refinement of previous hypotheses concerning the local structure of turbulence in a viscous incompressible fluid at high reynolds number, *Journal of Fluid Mechanics* **13**, 82–85 (1962).
- [38] J. de Jong, L. Cao, S. H. Woodward, J. P. L. C. Salazar, L. R. Collins, and H. Meng, Dissipation rate estimation from PIV in zero-mean isotropic turbulence, *Experiments in Fluids* **46**, 499 (2008).

- [39] D. Xu and J. Chen, Accurate estimate of turbulent dissipation rate using piv data, *Experimental Thermal and Fluid Science* **44**, 662 (2013).
- [40] K. Chang, G. P. Bewley, and E. Bodenschatz, Experimental study of the influence of anisotropy on the inertial scales of turbulence, *Journal of fluid mechanics* **692**, 464 (2012).
- [41] R. Zimmerman, H. Xu, Y. Gasteuil, M. Bourgoin, R. Volk, J.-F. Pinton, E. Bodenschatz, and I. C. for Turbulence Research, The lagrangian exploration module: An apparatus for the study of statistically homogeneous and isotropic turbulence, *Review of Scientific Instruments* **81**, 055112 (2010).
- [42] W. Hwang and J. Eaton, Creating homogeneous and isotropic turbulence without a mean flow, *Experiments in Fluids* **36**, 444 (2004).
- [43] C. Goepfert, J.-L. Marié, D. Chareyron, and M. Lance, Characterization of a system generating a homogeneous isotropic turbulence field by free synthetic jets, *Experiments in fluids* **48**, 809 (2010).
- [44] S. B. Pope, *Turbulent flows* (Cambridge University Press, Cambridge ; New York, 2000).
- [45] H. E. Cekli, C. Tipton, and W. van de Water, Resonant enhancement of turbulent energy dissipation, *Physical review letters* **105**, 044503 (2010).
- [46] R. A. Verschoof, A. K. te Nijenhuis, S. G. Huisman, C. Sun, and D. Lohse, Periodically driven taylor–couette turbulence, *Journal of fluid mechanics* **846**, 834 (2018).
- [47] R. H. Kraichnan, Helical turbulence and absolute equilibrium, *Journal of Fluid Mechanics* **59**, 745 (1973).
- [48] A. Alexakis, Helically decomposed turbulence, *Journal of Fluid Mechanics* **812**, 752 (2017), publisher: Cambridge University Press.
- [49] M. Gharib, E. Rambod, and K. Shariff, A universal time scale for vortex ring formation, *Journal of Fluid Mechanics* **360**, 121–140 (1998).
- [50] M. Raffel, C. E. Willert, F. Scarano, C. J. Kähler, S. T. Wereley, and J. Kompenhans, *Particle Image Velocimetry: A Practical Guide* (Springer International Publishing, 2018) oCLC: 1035110003.
- [51] A. Sciacchitano, F. Scarano, and B. Wieneke, Multi-frame pyramid correlation for time-resolved PIV, *Experiments in Fluids* **53**, 1087 (2012).
- [52] F. Scarano, Iterative image deformation methods in piv, *Measurement science and technology* **13**, R1 (2001).
- [53] D. Schanz, S. Gesemann, and A. Schröder, Shake-The-Box: Lagrangian particle tracking at high particle image densities, *Experiments in Fluids* **57**, 70 (2016).